ACCSCIENCE PUBLISHING

International Journal of Bioprinting

RESEARCH ARTICLE

A cylindrical slicing algorithm for four-axis non-planar bioprinting of complex geometries

Andrea Guerra[1,2†], Gabriele Maria Fortunato[1,2†], Amedeo Franco Bonatti[2], Giovanni Vozzi[1,2], and Carmelo De Maria[1,2*]

[1]Department of Information Engineering, School of Engineering, University of Pisa, Pisa, Italy

[2]Research Centre "E. Piaggio," University of Pisa, Pisa, Italy

Abstract

Additive manufacturing, particularly in bioprinting, relies on precise slicing algorithms to define printing paths. While traditional planar slicing methods impose geometric limitations, non-planar and multi-axis approaches have emerged to enhance surface quality and manufacturing efficiency. Among these, cylindrical slicing algorithms offer a novel strategy for optimizing material deposition on rotating mandrels. This study aims to implement a novel non-planar slicing algorithm capable of planning extrusion-based printing processes on a rotating mandrel. The algorithm partitions the initial volume into concentric cylindrical layers, each defined by an increasing radius around the mandrel's core. In the first step, the geometry is sectioned with a plane passing through the mandrel's axis and then unrolled to produce a volume lying on a planar face. This transformation, applicable to geometries regardless of axial symmetry, facilitates the application of conventional or custom planar/non-planar slicing algorithms. Subsequently, the calculated trajectories are rewrapped, transforming the planar layers into a series of coaxial cylindrical layers aligned around the mandrel. To validate the slicer's functionality, a rotating spindle was developed and integrated as a fourth motion axis into a previously designed multi-material, multi-scale 3D bioprinter. This system incorporates both an extrusion-based bioprinting unit and a fused filament fabrication unit. The algorithm enables full control over key printing parameters, such as layer thickness, layer width, and infill patterns. Testing on multiple 3D models relevant to biomedical applications demonstrated the algorithm's robust performance.

Keywords: Extrusion-based bioprinting; Four-axis bioprinter; Non-planar 3D Printing; Rotating mandrel; Slicing algorithm

†These authors contributed equally to this work.

***Corresponding author:**
Carmelo De Maria
(carmelo.demaria@unipi.it)

Citation: Guerra A, Fortunato GM, Bonatti AF, Vozzi G, Maria CD. A cylindrical slicing algorithm for four-axis non-planar bioprinting of complex geometries. *Int J Bioprint*. 2025;11(2):494-509. doi: 10.36922/IJB025070053

Received: February 10, 2025
1st revised: February 24, 2025
Accepted: February 25, 2025
Published Online: February 26, 2025

1. Introduction

Additive manufacturing (AM) encompasses a set of technologies used to fabricate objects from a digital model, offering the potential to reduce production times by up to 50%, even for highly complex parts.[1,2] In the field of tissue engineering (TE), AM techniques are referred to as bioprinting and are employed to produce complex three-dimensional (3D) bioconstructs that emulate native tissues and potentially entire organs. This is achieved through the layer-by-layer deposition of a mixture of cells, biomaterials, and

biomolecules.[3,4] The bioprinting process typically consists of four key steps: (i) designing a 3D model in a computer-aided design (CAD) environment; (ii) generating supports, slicing, and defining printing paths; (iii) layer-by-layer material deposition/solidification; and (iv) post-processing operations.[1,5] The most widely used bioprinting technologies include extrusion-based bioprinting (EBB), jetting-based bioprinting, and laser-based bioprinting.[6] EBB employs a pneumatic or mechanical system (piston- or screw-driven) to extrude a continuous filament of biomaterial ink or bioink through a nozzle.[7] Jetting-based bioprinting is a non-contact technique in which bioink droplets (ranging from picoliters to nanoliters) are deposited onto a substrate via thermal or piezoelectric actuation.[8] Among laser-based bioprinting techniques, the most commonly used is laser-induced forward transfer, in which a laser pulse transfers cells suspended in solution from a donor ribbon to a collector slide.[6] Recently, vat-photopolymerization-based technologies, such as stereolithography, two-photon polymerization, and digital light processing, have demonstrated the ability to fabricate structures with ultra-high resolution.[9]

A crucial step in AM is slicing, which directly impacts the accuracy and quality of the final print. Typically, the CAD model is exported as an .STL file, in which the volume is represented as a closed 3D tessellated surface composed of planar triangular elements [10,11] The conventional slicing approach, known as planar slicing, involves intersecting the .STL model with a series of horizontally stacked planes.[12] Each intersection generates closed curves or polygons that define individual slices, with slice thickness determined by the distance between the intersecting planes. Slice thickness directly influences both surface quality and build time; increasing slice spacing reduces print time but leads to the so-called stair-stepping effect, which degrades surface smoothness.[13] To improve print accuracy and structural integrity, various path-planning strategies have been developed over the years to generate printed structures that more closely resemble the original digital model. These advancements have significantly improved both the appearance and mechanical properties of printed objects.

In standard planar slicing, all layers maintain a constant thickness, which can limit surface quality and manufacturing efficiency, particularly in models with variable slopes. For regions with shallow slopes, thinner slices improve surface quality, while for near-vertical surfaces, thicker slices help reduce build time. Adaptive slicing—a technique that dynamically adjusts slice thickness based on local geometry—addresses this problem.[10,14–21] By significantly minimizing the stair-stepping effect, adaptive slicing reduces the discrepancy between the CAD model and the final 3D-printed structure.

Non-planar printing is a recent innovation designed to further improve surface quality and geometry accuracy.[22–25] Unlike traditional planar slicing, where slices are constrained to flat layers, non-planar slicing allows deposition paths to follow arbitrary 3D trajectories. However, while this approach enhances print quality, it significantly increases computational complexity, particularly in trajectory planning.[26,27] The first non-planar slicing method, known as curved layer fused deposition modeling (CLFDM),[28] involved dynamically modifying the z-values within individual layers. This approach allowed for smooth surfaces,[29] but was primarily limited to simple geometries with height variations restricted along the z-axis. Additionally, in regions with steep slopes, a collision risk arises between the deposited materials and the printer head, since the printer head cannot dynamically reorient itself. While early non-planar printing methods were applied to three-axis printing platforms, a more effective solution is to incorporate multi-axis printing systems.[30–32] Increasing the degrees of freedom (DoFs) in a printing system significantly reduces build times by eliminating the need for support structures (e.g., dynamically rotating the build axis to properly print overhanging features) while enabling the fabrication of highly complex geometries.[33] However, increasing the DoFs also introduces greater planning challenges due to the expanded workspace. The first proof-of-concept demonstration of multi-axis non-planar printing using fused deposition modeling (FDM) was conducted by Keating and Oxman,[34] who demonstrated improvements in the 3D printing process by utilizing all six DoFs of a robotic arm. However, their demonstration was limited to simple shapes, and no details were provided regarding toolpath generation. Pan et al.[35] later developed a five-axis platform that allowed material to be directly deposited onto an existing model. However, no robust planning system was introduced, and it could only handle components with relatively simple geometry. Recently, we developed a robust non-planar slicer capable of generating structures with non-planar surfaces on highly geometrically complex substrates by combining traditional planar layers with non-planar top and bottom layers.[36] This system was designed for applications requiring high *in situ* accuracy, such as *in situ* bioprinting techniques.[37] The algorithm was validated on the IMAGObot platform, a five-axis robotic platform equipped with an EBB tool,[38] but it can be easily adapted to any multi-axis printing system by modifying the kinetic parameters.

Both planar and non-planar slicing algorithms operate on the fundamental principle of stacking layers along a

specific growth direction, which may be either constant or variable. However, this approach becomes less efficient when the 3D printed part has a high aspect ratio between its non-staking dimensions (e.g., length significantly greater than width or height). A more effective solution would be to produce the part with radial growth around its primary dimension rather than along a single directional axis. Building on this concept, cylindrical slicing algorithms have been developed to partition the volume into concentrically arranged cylindrical layers with a progressively increasing radius. These algorithms naturally follow the object's shape, allowing for continuous and uniform deposition along helical or radial paths. In this approach, material deposition occurs on a rotating spindle (or another rotary support) rather than on a conventional print bed, thereby introducing an additional DoF.

In 2018, a pioneering study introduced an algorithm[39] (recently implemented in the MEWTube software[40]) for planning cylindrical prints to fabricate porous tubes using medical-grade poly(ε-caprolactone) for tissue engineering applications via the melt electro-writing (MEW) process. MEW is an AM technology that enables the direct and continuous deposition of molten polymer jets, stabilized by applying a voltage between the nozzle and the landing point of the fluid (collector).[41] Upon contact with the collector, the molten jet rapidly solidifies into a defined fiber with a small diameter (5–50 μm), which can be layered according to AM principles.[39,42] The developed software facilitates the planning of continuous direct writing paths required for MEW on a rotating cylindrical build surface. Although the software has proven highly effective for its intended application—enabling control over pore size, wrapping angle, and printing length—its functionality remains limited to fabricating tubular structures. Moreover, the algorithm cannot be generalized to accommodate geometries of different shapes or increased complexity.

A more generalizable cylindrical slicing algorithm was later developed.[43] This approach involved converting a traditional FDM Cartesian 3D printer into a cylindrical 3D printer by replacing the *y*-axis with a rotating cylinder. To enable printing on this platform, custom slicing software was developed to process .STL volumes using non-planar slicing techniques. This slicer was programmed in Python 3.7 using the numpy-stl library and the Panda3D Engine. The underlying concept is that replacing the printer's translational *y*-axis with a rotating cylinder causes conventional planar *y*-direction print commands to result in curved prints on the cylindrical surface. For example, instructing the printer to print a straight line in the *y*-direction results in a curved line on the rotating cylinder's surface, whereas printing a simple planar rectangle yields a cylindrical shell. Although this slicer performs well for relatively simple geometries, it has several limitations, including the inability to control infill percentage, layer orientation angle, and the relative alignment between layers. Furthermore, substituting a translational axis with a rotary one does not increase the printer's DoFs, thereby limiting its ability to fabricate more complex structures.

Building on these insights, the present study introduces a non-planar cylindrical slicing method designed to generate complex geometries using material extrusion processes. By integrating constant-radius cylindrical layers with variable-radius layers, the approach enhances surface quality. The algorithm is designed for use on any four-axis 3D printer (three Cartesian axes and one rotary axis), but it can be adapted to any multi-axis 3D printing platform with at least one rotary axis. The full code of the slicer, along with a user guide, has been released and is freely available on GitHub (https://github.com/CentroEPiaggio/4-axis-slicing- algorithm).

2. Materials and methods

2.1. Overview of the non-planar slicing algorithm

The slicer implemented in this study was developed entirely in Matlab® (The MathWorks Inc., United States) and enables the division of an initial volume into concentric cylindrical layers around a mandrel, rather than planar layers as in traditional slicing algorithms (Figure 1A and B). User inputs include the .STL volume to be printed (which can have an arbitrary shape without axial symmetry constraints) along with standard printing parameters used in traditional slicers, such as layer height, infill density, infill orientation, and the number of perimeters.

An important aspect of this approach is the pre-processing of the volume. Before slicing, the volume is virtually "unwrapped" around the mandrel (whose axis of symmetry is aligned with the *x*-axis and originates at $y = 0$) into a planar representation (Figure 2A and B). Following this transformation, a reconstruction phase ensures the generation of a closed, defect-free planar volume, which is then processed using an adapted version of a previously developed slicing algorithm.[38] This algorithm generates toolpaths consistent with the printing settings specified by the user (Figure 2C and D). After slicing, the generated trajectories are "rewound" around the mandrel by converting translational toolpath data into angular commands for the rotational printing axis (Figure 2E). Beyond constant-radius cylindrical layers, the algorithm also supports trajectories for variable-radius cylindrical

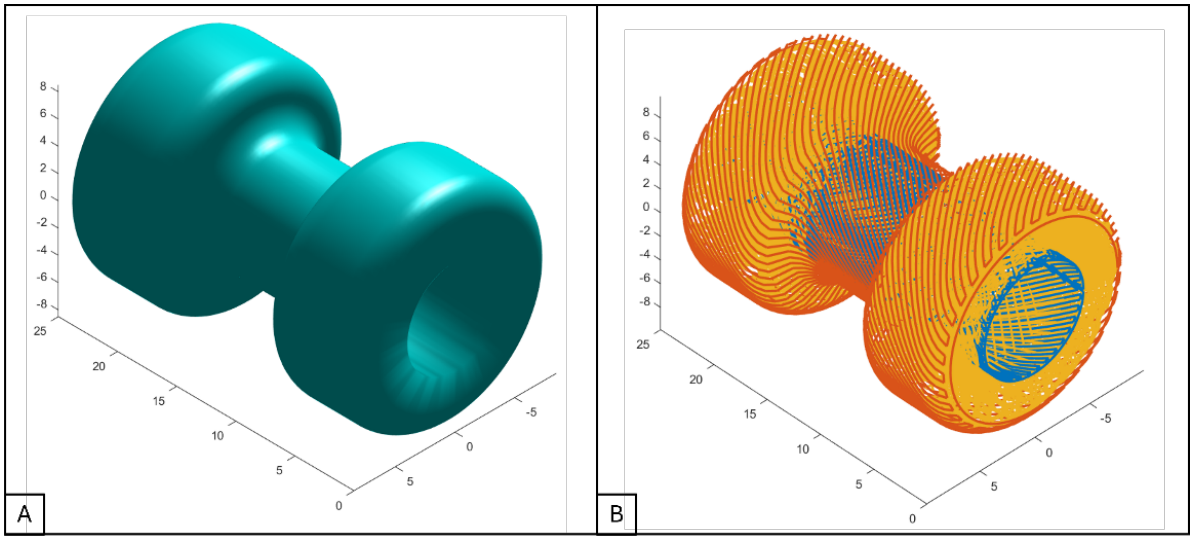

Figure 1. Schematic of the cylindrical slicer. (A) Sample object to be sliced. (B) Cylindrical layers generated by the algorithm.

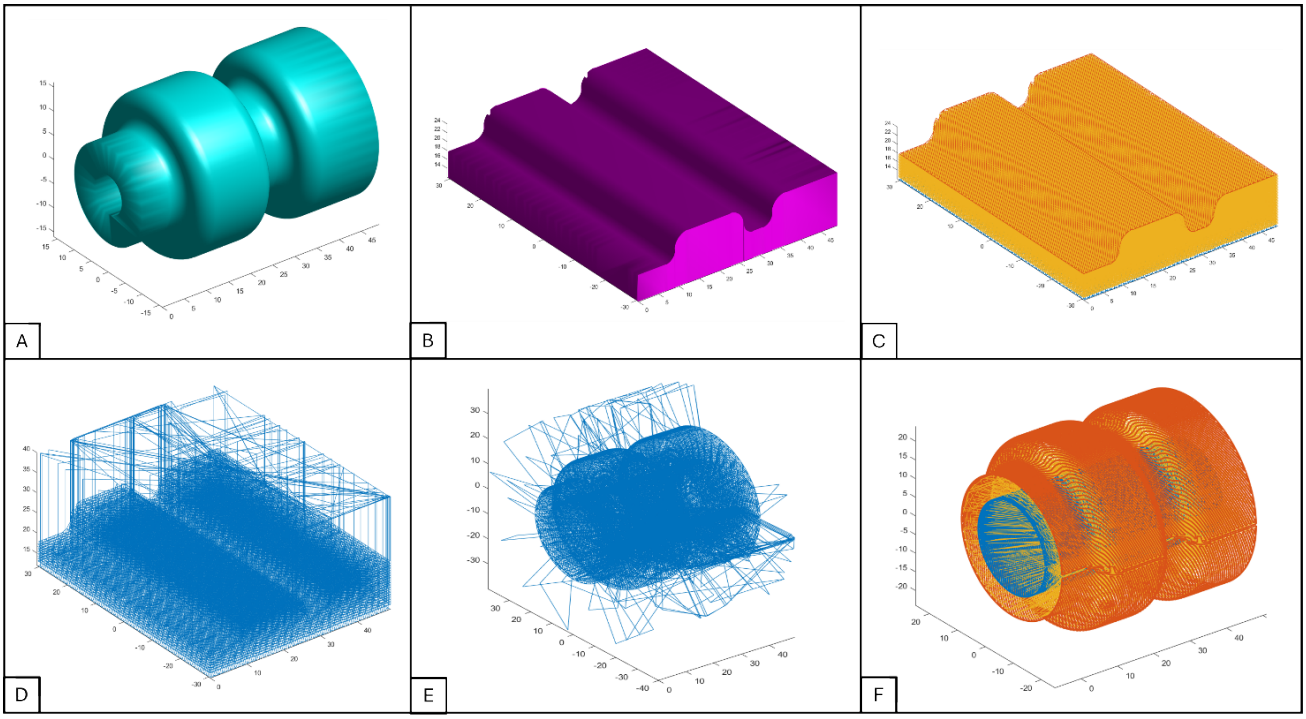

Figure 2. Cylindrical slicer pipeline. (A) Sample object to be sliced. (B) Unrolled and reconstructed volume. (C) Trajectories generated by the slicing algorithm. (D) Complete toolpath, including safety retraction. (E) Trajectories rewound around the cylinder. (F) External slices with a variable radius (in red).

layers (Figure 2F). This capability enhances surface quality by minimizing the stair-stepping effect and enables printing on complex, non-cylindrical rotating surfaces.

The final stage involves implementing controls for flow rate and printhead speed, along with strategies to prevent over-extrusion (e.g., retraction in the FDM printing). Upon

completing these procedures, the algorithm generates a dedicated G-code for cylindrical printing.

2.2. Algorithm implementation

2.2.1. Volume unwrapping

The first step of the algorithm is to generate a "flattened" version of the geometry, transforming it from a cylindrical shape around the mandrel to a planar representation. In the Matlab® implementation, this process involves modifying the spatial coordinates of the vertices in the .STL object provided by the user to achieve a planar representation. Once the .STL file is loaded, the algorithm extracts the vertex coordinates. These coordinates, initially expressed in Cartesian form (x, y, z), are transformed into cylindrical coordinates (x, θ, r), where θ is measured in radians within the range [−π, π]. Assuming a cylindrical volume oriented along the x-axis, the conversion is performed as follows (**Equations I and II**):

$$\theta = atan2\left(\frac{z}{y}\right) \quad \text{(I)}$$

$$r = \sqrt{y^2 + z^2} \quad \text{(II)}$$

At this stage, the volume is segmented along the x–r plane at the angular coordinate θ = π/−π (Figure 3A). To achieve this, the coordinates are remapped to a newly defined planar coordinate system (x_{new}, y_{new}, z_{new}), as **Equation (III)**:

$$\begin{pmatrix} x_{new} \\ y_{new} \\ z_{new} \end{pmatrix} = \begin{pmatrix} x \\ \theta \cdot r \\ r - r_{min} \end{pmatrix} \quad \text{(III)}$$

where x remains unchanged, while $\theta \cdot r$ translates the cylindrical angular position (θ) into a linear spatial position proportional to the radius. The term $r\text{-}r_{min}$ normalizes the cylindrical radius by offsetting it from r_{min}, thereby defining the new height of the volume. This transformation disrupts the face–vertex coherence of the .STL volume, necessitating a subsequent step to filter the faces and remap the vertices. Specifically, faces intersected by the cutting plane are identified and removed (Figure 3B). This operation ensures well-defined cut edges, effectively segregating faces on either side of the cutting plane.

After updating the faces, unused vertices are identified and eliminated, and a mapping is generated to reassign face indices to the revised vertex list. At this stage, the .STL volume has correctly unwrapped. However, the applied transformation creates an open volume at the regions intersected by the cutting plane (Figure 3C). As a result, the resulting volume is incompatible with slicing operations,

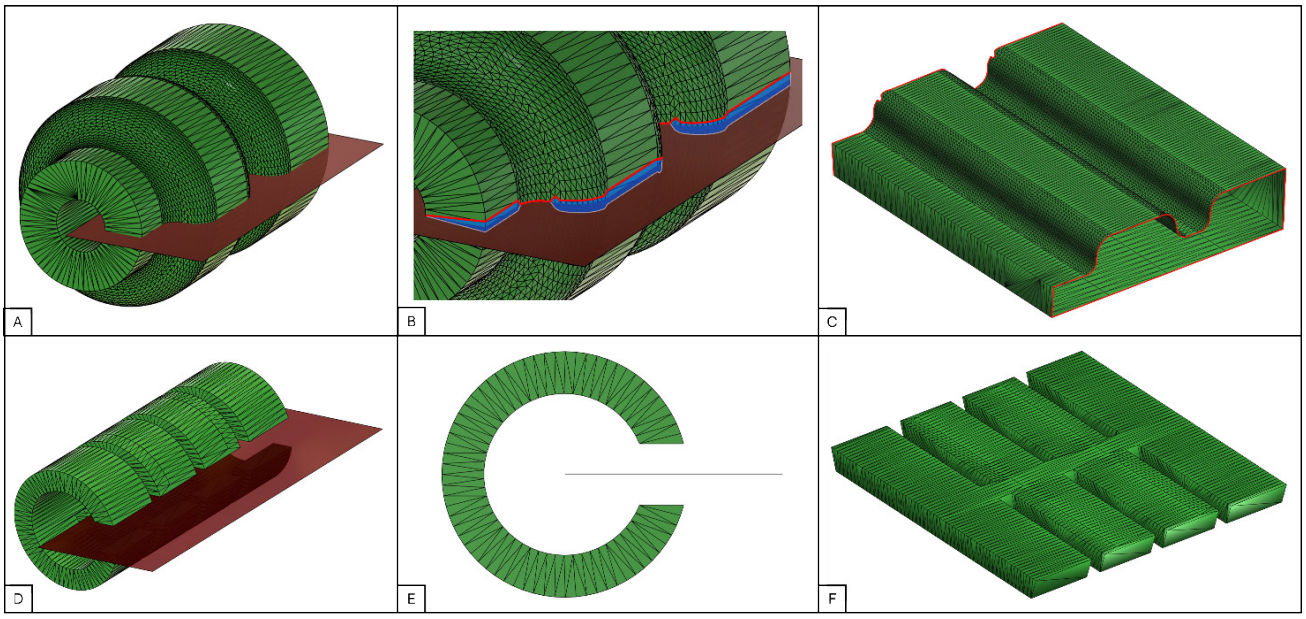

Figure 3. Cylindrical volume unwrapping. (A) Example of a volume to be unfolded and the cutting plane (red). (B) Triangular elements of the mesh intersecting the cutting plane and removed by the unwrapping algorithm (red highlights the cut volume's edge). (C) Unfolded volume with open ends (edges highlighted in red) due to the applied cut. (D) Example of a semi-closed shape (C-shaped) volume not intersecting the cutting plane. (E) Side view of the C-shaped volume. (F) Unfolded volume with closed ends.

necessitating an additional reconstruction phase to close it before proceeding to slicing.

Notably, when the initial geometry has a C-shape (i.e., no direct intersection with the cutting plane, as shown in Figure 3D and E), the transformation is limited to applying the mapping (**Equation III**) to the cylindrical coordinates. In this scenario, the resulting volume preserves face–vertex coherence and remains closed, eliminating the need for additional processing before slicing (Figure 3F).

2.2.2. Reconstruction of the unwrapped volume

Once the .STL volume has been unwrapped onto a plane with open ends, the next step is to create a closed volume compatible with the slicing process and, consequently, 3D printing.

To ensure robustness, a method was developed to isolate the upper surface of the flattened volume and regenerate a complete volume using projection techniques. The top surface is isolated by filtering faces according to the orientation of their normal vectors. Specifically, all faces whose normal component in the primary growth direction is greater than zero are classified as part of the top surface (Figure 4A and B).

Once the upper surface is isolated, projection algorithms are employed to reconstruct the volume beneath it. This step is performed using two distinct methods, chosen based on the geometric complexity of the initial upper surface. The complexity is defined by the number of isolated edges generated during surface isolation (Figure 4C). A greater number of edges increases the difficulty of volumetric reconstruction using projection methods.

If the number of isolated edges is two or fewer, reconstruction is performed using a computationally simpler approach based on the surf2solid function. This function takes as input the vertices and faces of the original upper surface and projects them along the z-axis. The projection is mapped onto a plane positioned at a distance of $-max(z_{new})$, corresponding to the maximum height of the unwrapped volume. This projection forms the lower surface of the volume, while the lateral surfaces are created by connecting the new surface to the original upper surface (Figure 4D). Upon completion, the function outputs a structure containing the resulting vertices and faces, which is then converted into a volume using the triangulation function. This process, implemented in Matlab,® mimics the solid extrusion operation found in CAD software but at a lower computational cost. However, if the initial surface is overly complex (i.e., containing more than two edges), the operation fails, resulting in a volume with inconsistent face–vertex relationships.

If the number of isolated edges exceeds two, a more computationally intensive reconstruction method is performed to overcome the limitations of the surf2solid function. This alternative method enables the solid extrusion of generic surfaces in Matlab,® regardless of their complexity. The first step involves generating the lower surface, either by projecting the upper surface along the z-axis (as in the surf2solid function) or by duplicating the upper surface, translating it to a different z-coordinate, and inverting the normal vector directions (Figure 4E). Next, the edges of the upper surface are identified by extracting the three edges of each face, compiling a list of all surface edges, and identifying those that appear only once as boundary edges. For each identified edge, triangular faces are constructed to connect the original and extruded vertices, forming the lateral surface of the volume. Finally, the original, translated, and lateral faces are combined to produce a closed solid.

After completing these steps, the distended volume is successfully reconstructed, and a .STL file is generated using the stlwrite function, ready for slicing.

2.2.3. Volume slicing

The model is sliced using a slicing algorithm developed in a previous study[38] for non-planar 3D printing applications. In summary, the algorithm first calculates the perimeters of each layer. The infill toolpath is then generated using a line pattern, with lines printed parallel to the x–y plane. A dedicated algorithm determines both the infill orientation—by rotating the external perimeter around the z-axis to align with the desired parallel orientation—and the infill density (e.g., an infill density of 100% connects all perimeter points, whereas a density of 50% connects only half). Furthermore, the algorithm supports the generation of non-planar upper and lower surfaces. These are initially defined as 2D surfaces and then projected onto the 3D model to determine the corresponding z-coordinates required for their construction (Figure 5A). Incorporating non-planar layers into the slicing process enables the creation of complex geometries with improved mechanical properties and superior surface quality compared to traditional planar slicing.

At this stage, the toolpath coordinates for each layer are "rewound" around the mandrel to reconstruct the original cylindrical geometry (Figure 5B and C). The degree of "overlap" between the two ends of the rewrapped volume can be adjusted. A 100% overlap reconstructs the original geometry, ensuring direct contact between the two ends. An overlap greater than 100% causes interpenetration, forming watertight surfaces, whereas an overlap below 100% results in a gap between the ends.

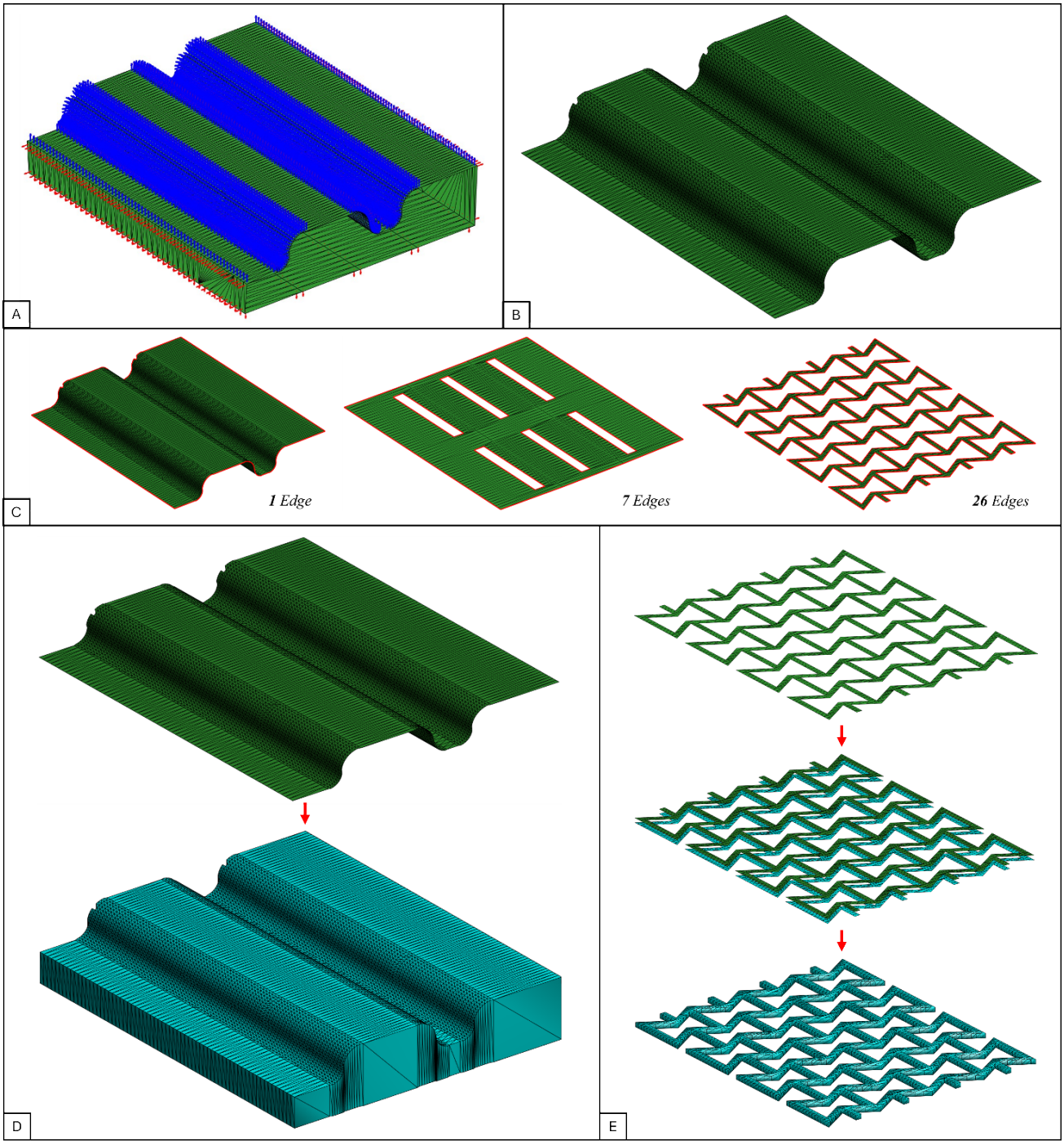

Figure 4. Reconstruction of the unwrapped volume. (A) Unrolled volume with normal vectors to the faces (blue vectors indicate the faces selected for surface isolation). (B) Isolated upper surface. (C) Examples of upper surfaces with increasing geometric complexity from left to right. (D) Volume reconstruction using the surf2solid algorithm. (E) Phases of volume reconstruction using the developed algorithm.

When slicing consists entirely of planar layers, each layer forms a cylindrical shell with a constant radius. The final geometry is constructed by stacking these layers while progressively increasing the radius (Figure 5D). Conversely, rewound non-planar layers form complex surfaces with variable radii, which are arranged around the mandrel (Figure 5E). These surfaces encapsulate the entire structure, significantly enhancing surface quality by eliminating the staircase effect inherent to horizontal layer-based manufacturing.

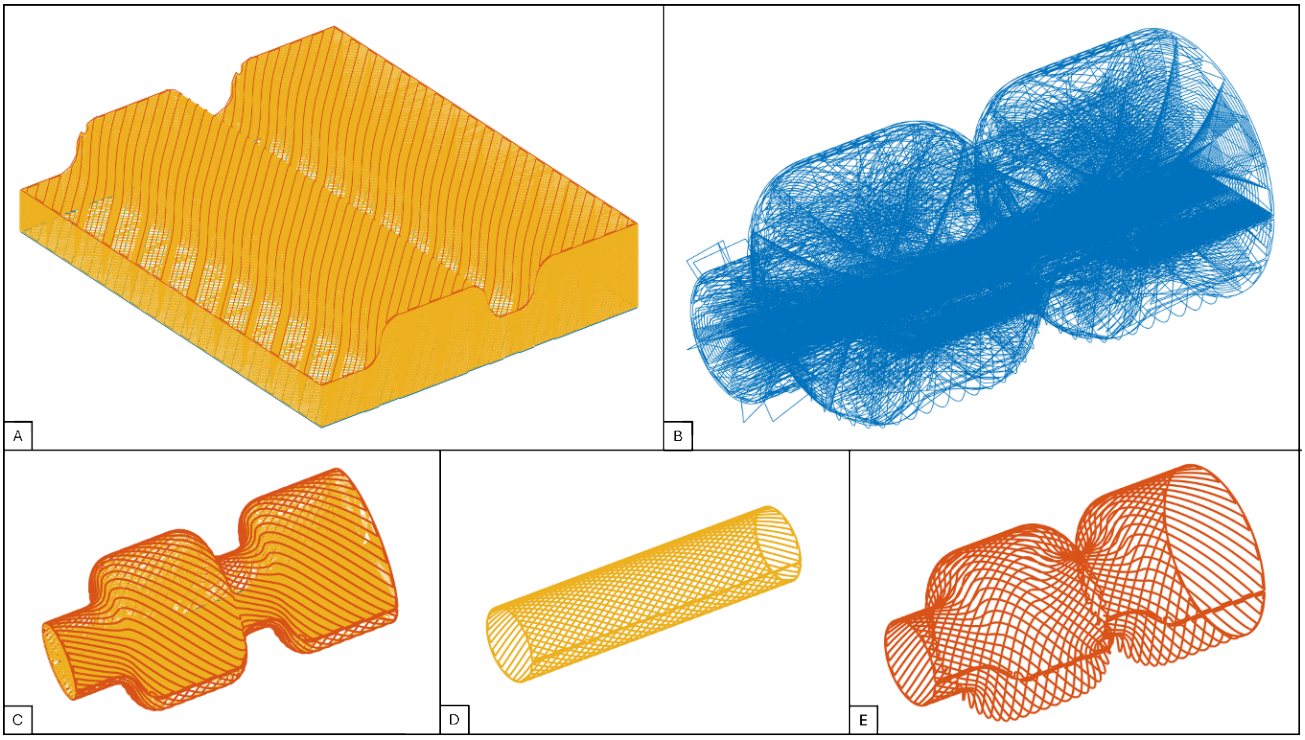

Figure 5. Volume slicing. (A) Print trajectories planned from the unrolled volume (upper non-planar layer in red). (B) Print trajectories rewound around the mandrel, with feedback movements at safety height visible during layer or path changes. (C) Rewound print trajectories, where constant-radius planar layers are in yellow, and the variable-radius surface layer is in red. (D) Example of an internal constant-radius layer. (E) External variable-radius cladding layer.

After computing the toolpaths, the resulting coordinates must be transformed for compatibility with the printing platform's control commands. This study utilized a previously developed multi-scale, multi-material 3D printing platform.[44] This platform, equipped with both an EBB and an FDM system, was modified to include an additional rotary axis. Cartesian axis commands specify the target position in millimeters, whereas rotary axis commands express the rotation angle in degrees. To ensure compatibility, the trajectory coordinates (x, y, z) are remapped to a new coordinate system (x_{fin}, φ_{fin}, z_{fin}), defined as follows (**Equation IV**):

$$\begin{pmatrix} x_{fin} \\ \varphi_{fin} \\ z_{fin} \end{pmatrix} = \begin{pmatrix} x \\ rad2\deg\left(\frac{y}{z}\right) \\ z \end{pmatrix} \quad \text{(IV)}$$

where x_{fin} remains unchanged, representing displacement along the cylindrical axis. z_{fin}, the height of the unwrapped volume, corresponds to the cylindrical structure's radius, dictating the nozzle-to-mandrel distance. φ_{fin}, derived from y/z, translates the linear spatial position of the unwrapped volume (originally in y) into an angular position expressed in degrees.

Finally, the 3D coordinate matrix of the calculated and transformed points, representing the cylindrical printing strategy on the rotating mandrel, is converted into a G-code. A specific G-code is generated based on the chosen printing technology (EBB or FDM). These codes differ in platform and extruder heating management, as well as in strategies to mitigate unwanted over-extrusion. This mitigation is necessary because, during printing, frequent trajectory changes require lifting the nozzle to a safe distance before repositioning. However, due to the viscoelasticity of the printed materials, extrusion continues momentarily after being halted, caused by spring-back effects. To mitigate this effect in FDM printing, a 6 mm retraction is applied when extrusion must be halted. For EBB printing, a gradual reduction in extrusion flow is implemented, beginning six points before the stop point. To further minimize this effect, non-extrusion movements are executed at a higher speed than printing movements. Notably, this algorithm segment is designed for easy adaptation to any printing machine with three or more DoFs, as long as at least one DoF is rotary.

2.3. Experimental validation

To experimentally validate the algorithm's performance, printing tests were performed using both EBB and FDM technologies. For EBB validation, a 20% w/v Pluronic F127 hydrogel (Sigma-Aldrich, Italy) was printed using a 21G needle (Metcal, Italy) at a linear speed of 3 mm/s. For FDM validation, a 1.75 mm polycaprolactone filament (Filoprint, Italy) was deposited at a linear speed of 3 mm/s. The following tests were conducted:

(i) FDM printing of an axisymmetric cylindrical structure with a variable-radius surface layer (80% infill for constant-radius layers, 100% for variable-radius layers, 200 μm layer thickness).

(ii) FDM printing of an auxetic stent, depositing only the perimeters (0% infill, 200 μm layer thickness)

(iii) FDM printing of a branched tubular structure, commonly found in vascular structures (80% infill, 200 μm layer thickness).

(iv) EBB printing of a branched tubular scaffold, commonly found in vascular structures (80% infill, 200 μm layer thickness).

The printing results were qualitatively analyzed to evaluate the potential of the proposed slicing algorithm, with a focus on improving surface characteristics, enabling the fabrication of complex geometries that are challenging for traditional 3D printers, and generating structures without the need for support materials. Additionally, a quantitative analysis was performed to evaluate the dimensional fidelity of the fabricated structures compared to their digital models (Figure 6A and C).

3. Results and discussion

3.1. Algorithm implementation

This section presents the results of the algorithm applied to structures intended for biomedical applications. Devices such as intravascular stents or vascular prostheses have complex geometries that are difficult to produce with traditional 3D printing techniques but are fully compatible with cylindrical printing.

The algorithm was tested on an intravascular stent model, a branched tubular structure, and a self-deploying bilayered scaffold (designed for 4D bioprinting) for tissue engineering applications, specifically in intestinal ulcer repair (Figure 7A, D, and G).

Printing directly on the lateral surface of a mandrel allows for the fabrication of these structures without the need for support in most cases. For example, complex structures such as vascular prosthesis branches or intricate networks of stents can be fabricated by directly depositing material onto the lateral surface of the rotating mandrel.

A comparison between the print preview calculated using our algorithm and that from traditional slicing software (e.g., Ultimaker Cura) shows that our approach results in simpler toothpaths and eliminates the need for support structures (Figure 7B, E, and H). In contrast, traditional slicers require support structures for geometries with cantilevered features, as they lack underlying material for stability (Figure 7C, F, and I). The inclusion of support structures reduces printing efficiency by increasing fabrication time, material waste, and the need for post-processing to remove residual supports.

Furthermore, the implementation of variable-radius layers covering the external surface of the printed object allows for the creation of a smooth contour that closely replicates the digital model. In traditional slicing software, these walls are generated by stacking multiple layers, resulting in rough surfaces due to the stair-stepping effect and increasing discretization errors as layer height increases. In contrast, our approach produces an outer surface consisting of a single continuous layer, ensuring greater surface homogeneity regardless of the underlying layer height.

The algorithm successfully sliced all geometries, regardless of their complexity. A critical aspect is the accurate reconstruction of the volume following the cutting and unfolding phases, as described in **Section 2.2.2**. In addition to the method described, alternative approaches can be used to "repair" damaged meshes or insert new faces and vertices to close holes or missing surfaces. For example, the .STL model can be exported and processed using mesh editing software such as Meshmixer (Autodesk®), MeshLab, or Blender. These software tools provide users with specific functionalities for identifying mesh defects and applying advanced reconstruction algorithms. However, this approach introduces a "manual" step into the printing preparation workflow, requiring the export of the volume from Matlab® and subsequent processing in external software. Since this study aims to develop fully automated slicing software, we prioritized using or developing tools that enable volume reconstruction directly within the Matlab® environment. Mesh hole reconstruction is not natively available in Matlab®; however, it can be implemented using standard surface reconstruction algorithms, potentially in combination with external toolboxes or libraries such as the MATLAB Mesh Processing Toolbox. Among commonly used surface reconstruction techniques (e.g., Delaunay Triangulation, Contour Averaging, Minimum Curvature, Local Projection,

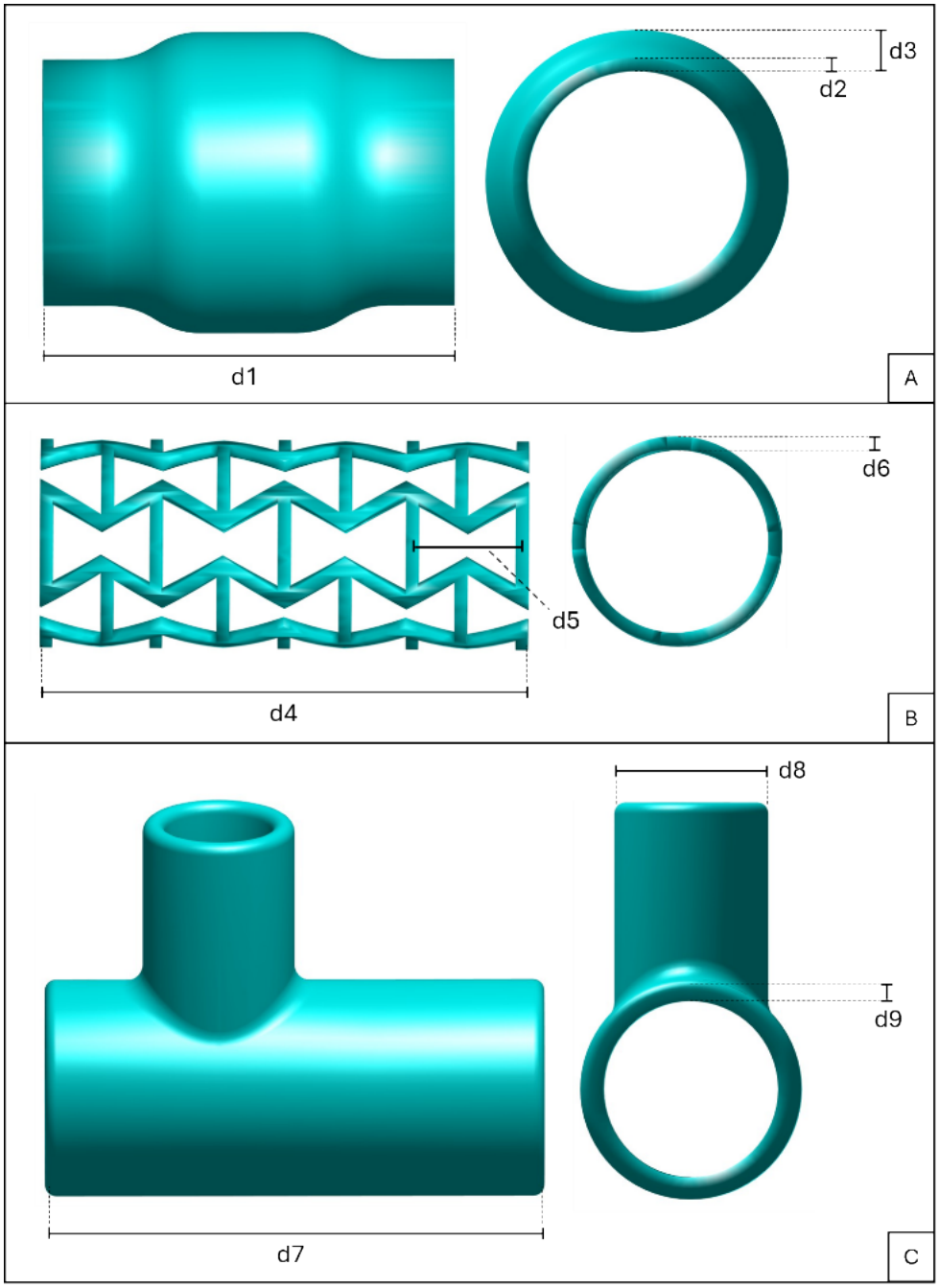

Figure 6. Geometric properties of the models. (A) Axisymmetric cylindrical structure: length (d1), thickness of the lateral zones (d2), and thickness of the central convex zone (d3). (B) Auxetic stent: length (d4), cell length (d5), and thickness (d6). (C) Branched tubular structure: length (d7), external diameter of the lateral branch (d8), and thickness (d9).

and Poisson Surface Reconstruction), only Delaunay Triangulation and Poisson Surface Reconstruction have dedicated functions or libraries in Matlab.® For instance, the Delaunay Triangulation function constructs 2D or 3D triangulated surfaces from a set of spatial points, while the pc2surface mesh function generates a surface mesh from an input point cloud using the Poisson Surface Reconstruction method. However, these algorithms are primarily designed for surface reconstruction from point clouds. While they may be effective in repairing small holes in the mesh, they exhibit significant limitations when applied to the specific case discussed here.

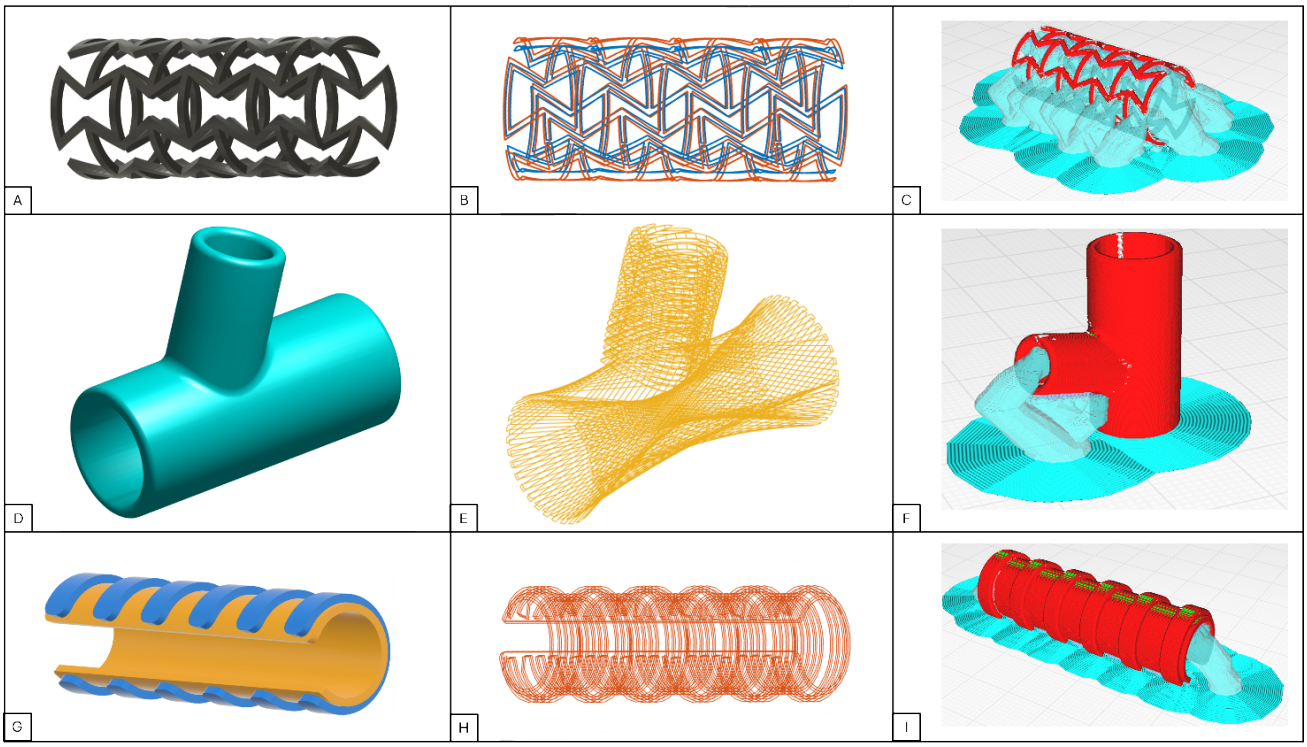

Figure 7. Printing planning. (A) 3D model of an intravascular stent. (B) Printing trajectories generated using the cylindrical slicer. (C) Printing trajectories generated with a traditional slicer (numerous supports are required to stabilize the part). (D) 3D model of a branched tubular structure common in vascular applications. (E) Printing trajectories generated using the cylindrical slicer, where both the main cylinder and the lateral branching are fabricated without supports. (F) Traditional slicing-generated trajectories requiring support due to cantilevered branching. (G) Self-deploying bilayered scaffold for tissue engineering applications in intestinal ulcer repair. (H) Cylindrical trajectories developed around the rotating mandrel. (I) Traditional slicing-generated trajectories, where the C-shaped cylindrical structure would collapse without internal supports.

For the open ends of the volume, only perimeter points are available, whereas effective reconstruction would typically require internal points as well. Furthermore, the open ends can be relatively large (Figure 3D), complicating reconstruction due to the limited number of available starting points.

Therefore, the cylindrical slicing software is robust and capable of planning printing trajectories for 3D models with any level of geometric complexity, including holes and lateral branches. Furthermore, for concave or convex surfaces, the ability to generate variable-radius layers allows for trajectory planning that conforms precisely to the actual geometry of the model, maximizing homogeneity and geometric fidelity.

3.2. Experimental validation

The algorithm was experimentally tested to evaluate its ability to print geometries of varying complexity (see Videos S1–S4, Supporting Information).

The first FDM print test was conducted to create an axially symmetric geometry with a convex lateral surface (Figure 8A), focusing on generating external surfaces with variable radii (Figure 8B–D). The structure was printed with 100% infill to ensure structural robustness and a smooth outer surface. The printer trajectories faithfully matched the planned toothpaths, demonstrating the robustness of the algorithm.

In the second FDM printing test, an intravascular stent model was fabricated (Figure 8E). The non-axially symmetric geometry features a lattice structure that is too complex to fabricate using traditional 3D printing techniques. However, using the cylindrical printing approach, the desired geometry was easily obtained by depositing two constant-radius layers (200 μm layer thickness). A 0% infill was chosen for this test, depositing only the structure's perimeters (Figure 8F–H).

The third FDM print test involved fabricating a tubular structure designed to simulate branched geometries, such as blood vessels (Figure 8I). Furthermore, this geometry demonstrated how the cylindrical slicer simplifies the fabrication of overhanging features (e.g., lateral branching),

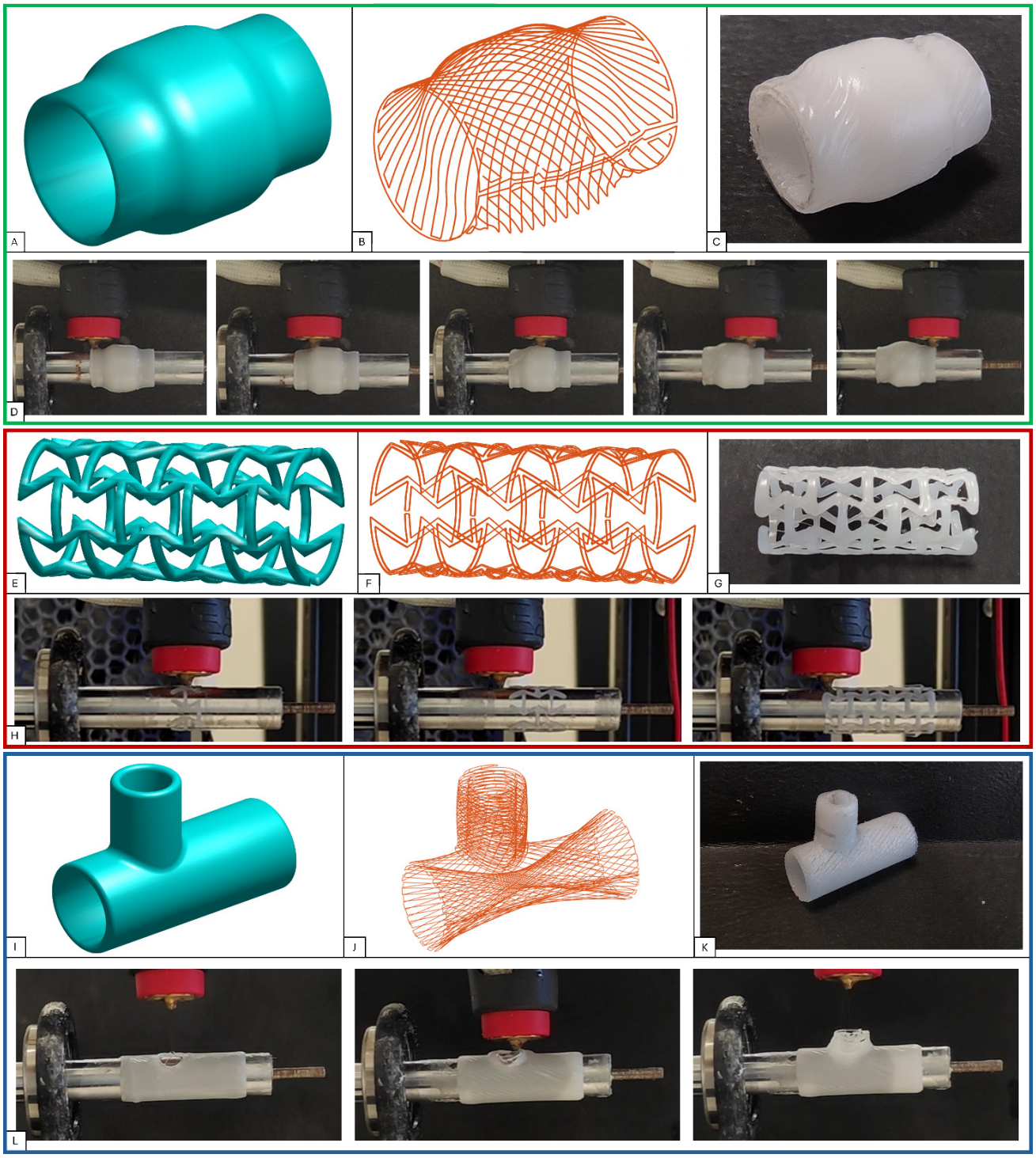

Figure 8. Cylindrical fused deposition modeling printing results. (A) 3D model of the object to be printed. (B) Printing trajectories for the outermost layer with a variable radius. (C) Final printed product: filament lines are visible and closely follow the planned trajectory. (D) Printing process: the printer nozzle dynamically adjusts its distance from the mandrel based on the radius of the planned cylindrical trajectory. (E) 3D model of a cardiovascular stent. (F) Generated trajectories, showing only perimeters without infill. (G) Fabricated stent. (H) Printing process: material is deposited on the lateral surface of the mandrel without requiring support. (I) 3D model of a branched structure. (J) Generated constant-radius trajectories. (K) The final printed piece, produced without support structures. (L) Printing process: after forming the main channel, the lateral branching is printed layer by layer.

Table 1. Comparison of digital model (M) and printed structure (P) dimensions

Parameters	d1 (mm)	d2 (mm)	d3 (mm)	d4 (mm)	d5 (mm)	d6 (mm)	d7 (mm)	d8 (mm)	d9 (mm)
M	15.00	0.50	1.50	20.00	5.20	0.40	23.00	0.60	7.00
P	14.94±0.13	0.52±0.02	1.54±0.03	20.35±0.11	5.01±0.08	0.41±0.01	23.27±0.11	0.59±0.01	7.04±0.09

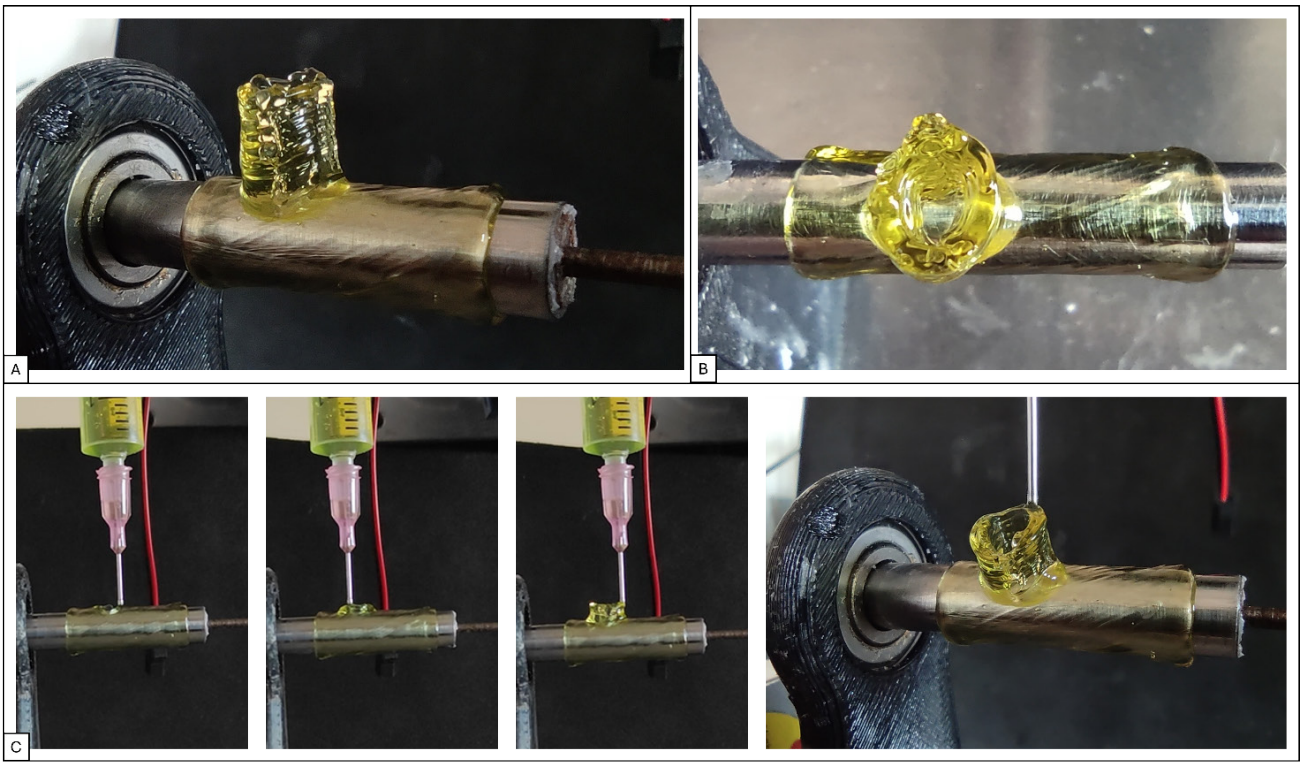

Figure 9. Cylindrical extrusion-based bioprinting printing results. (A) Final printed product. (B) The central channel of the lateral branch, demonstrating an open structure that maintains its integrity. (C) Printing process: after depositing the first cylindrical layers to create the main branch, the lateral branch is formed by depositing material layer by layer with an increasing radius. As it develops radially, no supports are required.

which traditionally require internal and external supports. In this case, the lateral branch was developed radially by stacking layers with progressively increasing radii (Figure 8J–L).

The average width of the printed lines was 415 ± 16 μm. For each printed structure, dimensions were evaluated by comparing them to the original digital model (Figure 6A–C). As reported in Table 1, mandrel-based printing successfully fabricated various geometries with acceptable deviations from the expected dimensions.

The same geometry from the third FDM printing test was also used to validate the slicing algorithm for EBB printing. EBB printing primarily involves the extrusion of hydrogel materials (e.g., alginate, Pluronic F127, gelatin). In this test, the structure was bioprinted using 20% w/v Pluronic F127.[45,46] The structure was fabricated without the need for support (Figure 9A) and maintained its integrity, neither collapsing nor occluding the central channel (Figure 9B and C). For proper processing in EBB, hydrogels must exhibit a non-zero yield stress (e.g., 500 Pa for Pluronic F127) to prevent collapse under their own weight.[47–50] Mandrel printing significantly simplifies the fabrication of complex structures that are challenging to produce using traditional techniques and would otherwise require gel-in-gel approaches, also known as embedded bioprinting. Although embedded bioprinting enables the fabrication of highly complex structures, it is a time-consuming process. Additionally, removing the support gel can be challenging, and residual gel trapped between layers may cause delamination. In contrast, mandrel-printable structures streamline fabrication by allowing material deposition directly onto the lateral surface of

a rotating mandrel, eliminating the need for extensive support structures.

4. Conclusion

This presented a new non-planar slicing algorithm capable of generating cylindrical 3D trajectories with both constant and non-constant radii. To achieve this, the object to be reconstructed is cut and unrolled from its initial shape. Slicing is performed on the deformed model, and the resulting trajectories are subsequently rewound into a cylindrical configuration. This algorithm can slice geometries of any complexity and represents a significant advancement in planning printing on rotating elements compared to previously developed algorithms. Notably, the algorithm allows for the fabrication of complex structures without requiring support material, irrespective of surface textures or lateral branching. Furthermore, the introduction of variable-radius layers enhances both esthetic and functional properties, completely eliminating the stair-stepping effect. The algorithm was successfully validated using a multi-scale, multi-material 3D printing platform, which was re-engineered to include an additional rotary axis and is equipped with both EBB and FDM systems. In the future, the proposed algorithm will be adapted for additional bioprinting technologies, such as inkjet printing, which is also well suited for rotating mandrel printing, enabling the precise deposition of bioink droplets onto or into cylindrical structures.

Acknowledgments

None

Funding

The authors received funding from the European Union - Next Generation EU, Mission 4 - Component 1 (CUP I53D23002200006), through the Prin2022 Prometheus project, "4D printing self-deploying bio-enabled polymer scaffolds for the non-invasive treatment of bleeding intestinal ulcers" (grant no.: 2022BZLTTK). Additional funding was provided by the European Union - Next Generation EU, Mission 4 - Component 2, Investment 1.5 (CUP I53C22000780001) under the Tuscany Health Ecosystem, Spoke 4: Nanotechnologies for diagnosis and therapy. This work was also partially supported by the Italian Ministry of Education and Research (MUR) within the framework of the FoReLab and CrossLab projects (Departments of Excellence).

Conflict of interest

Gabriele Maria Fortunato, Giovanni Vozzi, and Carmelo De Maria serve as the Editorial Board Members of the journal, but were not in any way involved in the editorial and peer-review process conducted for this paper, directly or indirectly. Other authors declare they have no competing interests.

Author contributions

Conceptualization: Gabriele Maria Fortunato, Carmelo De Maria
Formal analysis: Giovanni Vozzi, Carmelo De Maria
Investigation: Andrea Guerra, Amedeo Franco Bonatti
Methodology: Gabriele Maria Fortunato, Amedeo Franco Bonatti, Andrea Guerra
Writing – original draft: Andrea Guerra, Gabriele Maria Fortunato
Writing – review & editing: Carmelo De Maria

Ethics approval and consent to participate

Not applicable.

Consent for publication

Not applicable.

Availability of data

Data are available upon reasonable request. Algorithms are available on https://github.com/CentroEPiaggio/4-axis- slicing-algorithm.

References

1. Mohan Pandey P, Venkata Reddy N, Dhande SG. Slicing procedures in layered manufacturing: a review. *Rapid Prototyp J*. 2003;9(5):274-288. doi: 10.1108/13552540310502185
2. Chua CK, Leong KF, Lim CS. *Rapid Prototyping: Principles and Applications*. World scientific; 2010. doi: 10.1142/6665
3. Zhu W, Ma X, Gou M, Mei D, Zhang K, Chen S. 3D printing of functional biomaterials for tissue engineering. *Curr Opin Biotechnol*. 2016;40:103-112. doi: 10.1016/j.copbio.2016.03.014
4. Langer R, Vacanti J. Advances in tissue engineering. *J Pediatr Surg*. 2016;51(1):8-12. doi: 10.1016/j.jpedsurg.2015.10.022
5. Sathies T, Senthil P, Anoop MS. A review on advancements in applications of fused deposition modelling process. *Rapid Prototyp J*. 2020;26(4):669-687. doi: 10.1108/RPJ-08-2018-0199
6. Dababneh AB, Ozbolat IT. Bioprinting technology: a current state-of-the-art review. *J Manuf Sci Eng*. 2014;136(6): 061016.

doi: 10.1115/1.4028512

7. Naghieh S, Chen X. Printability–a key issue in extrusion-based bioprinting. *J Pharm Anal*. 2021;11(5):564-579. doi: 10.1016/j.jpha.2021.02.001
8. Ng WL, Shkolnikov V. Jetting-based bioprinting: process, dispense physics, and applications. *Biodes Manuf*. 2024;7(5):771-799. doi: 10.1007/s42242-024-00285-3
9. Lu Z, Gao W, Liu F, et al. Vat photopolymerization based digital light processing 3D printing hydrogels in biomedical fields: key parameters and perspective. *Addit Manuf*. 2024;94:104443. doi: 10.1016/j.addma.2024.104443
10. Sun SH, Chiang HW, Lee MI. Adaptive direct slicing of a commercial CAD model for use in rapid prototyping. *Int J Adv Manuf Technol*. 2007;34(7):689-701. doi: 10.1007/s00170-006-0651-y
11. Zhao Z, Laperriere L. Adaptive direct slicing of the solid model for rapid prototyping. *Int J Prod Res*. 2000;38(1):69-83. doi: 10.1080/002075400189581
12. Xu J, Gu X, Ding D, Pan Z, Chen K. A review of slicing methods for directed energy deposition based additive manufacturing. *Rapid Prototyp J*. 2018;24(6):1012-1025. doi: 10.1108/RPJ-10-2017-0196
13. Minetto R, Volpato N, Stolfi J, Gregori RMMH, Da Silva MVG. An optimal algorithm for 3D triangle mesh slicing. *Computer-Aided Design*. 2017;92:1-10. https://doi.org/10.1016/j.cad.2017.07.001
14. Tata K, Fadel G, Bagchi A, Aziz N. Efficient slicing for layered manufacturing. *Rapid Prototyp J*. 1998;4(4):151-167. doi: 10.1108/13552549810239003
15. Tata K, Fadel G. Feature Extraction from Tessellated and Sliced Data in Layered Manufacturing; 1996. http://hdl.handle.net/2152/70294
16. Kulkarni P, Dutta D. Adaptive slicing of parametrizable algebraic surfaces for layered manufacturing. In: *International Design Engineering Technical Conferences and Computers and Information in Engineering Conference*. Vol 17162. American Society of Mechanical Engineers; 1995:211-217. doi: 10.1115/DETC1995-0028
17. Suh YS, Wozny MJ. Adaptive Slicing Of Solid Freeform Fabrication Processes; 1994. http://hdl.handle.net/2152/68677
18. Sreeram PN, Dutta D. Determination of optimal orientation based on variable slicing thickness in layered manufacturing. In: *Proceedings of the 1995 ASME Winter Annual Conference*; 1995.
19. Dolenc A, Mäkelä I. Slicing procedures for layered manufacturing techniques. *Computer-Aided Design*. 1994;26(2):119-126. doi: 10.1016/0010-4485(94)90032-9
20. Lee KH, Choi K. Generating optimal slice data for layered manufacturing. *Int J Adv Manuf Technol*. 2000;16(4):277-284. doi: 10.1007/s001700050157
21. Sabourin E, Houser SA, Helge Bøhn J. Adaptive slicing using stepwise uniform refinement. *Rapid Prototyp J*. 1996;2(4):20-26. doi: 10.1108/13552549610153370
22. Ahlers D, Wasserfall F, Hendrich N, Zhang J. 3D printing of nonplanar layers for smooth surface generation. In: *2019 IEEE 15th International Conference on Automation Science and Engineering (CASE)*. IEEE; 2019:1737-1743. doi: 10.1109/COASE.2019.8843116
23. Nisja GA, Cao A, Gao C. Short review of nonplanar fused deposition modeling printing. *Mater Design Process Commun*. 2021;3(4):e221. doi: 10.1002/mdp2.221
24. Cendrero AM, Fortunato GM, Munoz-Guijosa JM, De Maria C, Díaz Lantada A. Benefits of non-planar printing strategies towards eco-efficient 3d printing. *Sustainability*. 2021;13(4):1599. doi: 10.3390/su13041599
25. Shahid ST. Modeling of non-planar slicer for improved surface quality in material extrusion 3D printing. *arXiv preprint arXiv:241107225*; 2024. doi: 10.48550/arXiv.2411.07225
26. Shembekar AV, Yoon YJ, Kanyuck A, Gupta SK. Trajectory planning for conformal 3d printing using non-planar layers. In: *International Design Engineering Technical Conferences and Computers and Information in Engineering Conference*. Vol 51722. American Society of Mechanical Engineers; 2018:V01AT02A026. doi: 10.1115/DETC2018-85975
27. Atarihuana S, Fernández F, Erazo J, Narváez M, Hidalgo V. Optimal strategies for filament orientation in non-planar 3D printing. *Processes*. 2024;12(12):2811. doi: 10.3390/pr12122811
28. Chakraborty D, Reddy BA, Choudhury AR. Extruder path generation for curved layer fused deposition modeling. *Computer-Aided Design*. 2008;40(2):235-243. doi: 10.1016/j.cad.2007.10.014
29. Llewellyn-Jones T, Allen R, Trask R. Curved layer fused filament fabrication using automated toolpath generation. *3D Print Addit Manuf*. 2016;3(4):236-243. doi: 10.1089/3dp.2016.0033
30. Rodriguez-Padilla C, Cuan-Urquizo E, Roman-Flores A, Gordillo JL, Vázquez-Hurtado C. Algorithm for the conformal 3D printing on non-planar tessellated surfaces: Applicability in patterns and lattices. *Appl Sci*. 2021;11(16):7509. doi: 10.3390/app11167509

31. Yao Y, Cheng L, Li Z. A comparative review of multi-axis 3D printing. *J Manuf Process*. 2024;120:1002-1022. doi: 10.1016/j.jmapro.2024.04.084

32. Patil AS. *Fabrication of Nonplanar Surfaces Via 5-Axis 3D Printing*. Rochester Institute of Technology; 2022.

33. Dai C, Wang CCL, Wu C, Lefebvre S, Fang G, Liu YJ. Support-free volume printing by multi-axis motion. *ACM Trans Graph*. 2018;37(4):1-14. doi: 10.1145/3197517.3201342

34. Keating S, Oxman N. Compound fabrication: a multi-functional robotic platform for digital design and fabrication. *Robot Comput Integr Manuf*. 2013;29(6):439-448. doi: 10.1016/j.rcim.2013.05.001

35. Pan Y, Zhou C, Chen Y, Partanen J. Multitool and multi-axis computer numerically controlled accumulation for fabricating conformal features on curved surfaces. *J Manuf Sci Eng*. 2014;136(3):031007. doi: 10.1115/1.4026898

36. Fortunato GM, Nicoletta M, Batoni E, Vozzi G, De Maria C. A fully automatic non-planar slicing algorithm for the additive manufacturing of complex geometries. *Addit Manuf*. 2023;69:103541. doi: 10.1016/j.addma.2023.103541

37. Samandari M, Mostafavi A, Quint J, Memić A, Tamayol A. In situ bioprinting: intraoperative implementation of regenerative medicine. *Trends Biotechnol*. 2022;40(10):1229-1247. doi: 10.1016/j.tibtech.2022.03.009

38. Fortunato GM, Rossi G, Bonatti AF, et al. Robotic platform and path planning algorithm for in situ bioprinting. *Bioprinting*. 2021;22:e00139. doi: 10.1016/j.bprint.2021.e00139

39. McColl E, Groll J, Jungst T, Dalton PD. Design and fabrication of melt electrowritten tubes using intuitive software. *Mater Des*. 2018;155:46-58. doi: 10.1016/j.matdes.2018.05.036

40. McColl E, Groll J, Jungst T, Dalton DP. MEWtubes; 2018. Accessed November 28, 2024. http://mewtubes.herokuapp.com/

41. Dalton PD. Melt electrowriting with additive manufacturing principles. *Curr Opin Biomed Eng*. 2017;2:49-57. doi: 10.1016/j.cobme.2017.05.007

42. Saidy NT, Shabab T, Bas O, et al. Melt electrowriting of complex 3D anatomically relevant scaffolds. *Front Bioeng Biotechnol*. 2020;8:793. doi: 10.3389/fbioe.2020.00793

43. Vandenberghe L. Angl3dprinting; 2020. Accessed November 28, 2024. https://github.com/vandenbergheluke/cylindrical-slicer/tree/main

44. Bonatti AF, Batoni E, Fortunato GM, Vitale-Brovarone C, Vozzi G, De Maria C. Robust design methodologies to engineer multimaterial and multiscale bioprinters. *Bioprinting*. 2024;44:e00372. doi: 10.1016/j.bprint.2024.e00372

45. Bonatti AF, Chiesa I, Vozzi G, De Maria C. Open-source CAD-CAM simulator of the extrusion-based bioprinting process. *Bioprinting*. 2021;24:e00172. doi: 10.1016/j.bprint.2021.e00172

46. Nascimento MHM, Franco MKKD, Yokaichyia F, de Paula E, Lombello CB, de Araujo DR. Hyaluronic acid in pluronic F-127/F-108 hydrogels for postoperative pain in arthroplasties: influence on physico-chemical properties and structural requirements for sustained drug-release. *Int J Biol Macromol*. 2018;111:1245-1254. doi: 10.1016/j.ijbiomac.2018.01.064

47. Boluk Y, Lan X, Adesida A. Additive manufacturing by Gel-in-Gel printing. *Annu Trans Nordic Rheol Soc*. 2024;32:157-161. doi: https://doi.org/10.31265/atnrs.778

48. Hinton TJ, Jallerat Q, Palchesko RN, et al. Three-dimensional printing of complex biological structures by freeform reversible embedding of suspended hydrogels. *Sci Adv*. 2015;1(9):e1500758. doi: 10.1126/sciadv.1500758

49. Chiesa I, De Maria C, Lapomarda A, et al. Endothelial cells support osteogenesis in an in vitro vascularized bone model developed by 3D bioprinting. *Biofabrication*. 2020;12(2):025013. doi: 10.1088/1758-5090/ab6a1d

50. De Maria C, Chiesa I, Morselli D, et al. Biomimetic tendrils by four dimensional printing bimorph springs with torsion and contraction properties based on bio-compatible graphene/silk fibroin and poly (3-hydroxybutyrate-co-3-hydroxyvalerate). *Adv Funct Mater*. 2021;31(52):2105665. https://doi.org/10.1002/adfm.202105665